In-Situ Hot Stage Atomic Force Microscopy Study of Poly(ϵ-caprolactone) Crystal Growth in Ultrathin Films

Vincent H. Mareau and Robert E. Prud'homme*

Department of Chemistry, CERSIM, Laval University, Québec, Canada G1K 7P4, and Department of Chemistry, University of Montréal, Montréal, Canada H3C 3J7

Received August 28, 2004; Revised Manuscript Received November 2, 2004

ABSTRACT: Morphologies, growth rates, and melting of isothermally crystallized ultrathin (200−1 nm) poly(ϵ-caprolactone) (PCL) films have been investigated in real time by atomic force microscopy. The flat-on orientation of the lamellar crystals relative to the substrate was determined by electron diffraction. The truncated lozenge-shaped PCL crystals observed at low undercooling become distorted for films of thicknesses equal to or thinner than the lamellar thickness, which depends on the crystallization temperature but not on the initial film thickness. The melting behavior of distorted crystals differs from that of undistorted ones, and their growth is slower and nonlinear. The crystal growth rate decreases greatly with the film thickness. All these observations are discussed in terms of the diffusion of the polymer chains from the melt to the crystal growth front.

Introduction

Since the initial in-situ observations of the crystallization of polymers from the melt by hot stage atomic force microscopy (AFM) reported by Pearce and Vancso,[1−3] and almost simultaneously by Schultz and Miles,[4] several additional real-time AFM studies were published.[5−25] Some of these studies were done at ambient temperatures, with polymers crystallizing slowly enough to allow the observation,[5−10] whereas others were performed by controlling the temperature of the sample[11−25] and sometimes of the AFM tip.[20−22]

Pearce and Vancso[1,2] first reported the consistency of in-situ AFM results with conventional optical microscopy results. They found that growth rates of individual lamellae agree with results obtained at lower magnification by optical microscopy. Similar growth rates were observed at the growth front by Hobbs et al.,[8] whereas observations at the scale of the lamella revealed for the first time that dominant lamellae do not grow at a constant rate. Later in-situ observations of polyethylene shish-kebab crystals[24] confirmed those variations of growth rates at the lamellar scale, challenging theories of polymer crystallization.[26] Lamellae propagating at sporadic rates were also observed by Li et al.[6,7] in thin films of poly(bisphenol A-*co*-octane), but additional experiments on the same polymer gave contradictory results, with lamellae growing at a constant rate.[10] Apparently, lamellae grow at sporadic or constant rates depending on the presence or not of surrounding lamellae competing at the growth front. This could explain why constant growth rates were always reported by in-situ AFM studies of melt-grown single crystals.[10−17,25]

In-situ AFM studies gave for the first time the opportunity to observe developing spherulites at a lamellar scale, from the generation of the primary stable nucleus[6,7,9,10,19] to the development of dominant lamellae, followed by the creation of induced nucleus[6,7,9,20] or screw dislocations[4,17] giving birth to branching lamellae that splay, leading to the spherulitic morphology[2−4,6,10] with, finally, impingement of adjacent spherulites.[3] These observations highlighted the roughness of the growth front, seen as being smooth at the larger scale of optical microscopy.[8] Real-time AFM imaging of the secondary crystallization was shown to be very efficient and complementary to time-resolved small-angle X-ray scattering (SAXS) in the study of a semicrystalline/amorphous polymer blend[23] and to explain the stack thickening process, seen by SAXS, taking place during the secondary crystallization of poly(ethylene terephthalate).[21]

In the articles cited above, the thickness of the polymer films is often less than 1 μm (thin films) and sometimes less than 100 nm (ultrathin films). Hot stage AFM being a nondestructive technique with a high spatial resolution, it has become one of the most powerful tools available to study the crystallization of ultrathin polymer films. In addition, such polymer films are good model systems to achieve a better understanding of the fundamentals of polymer crystallization,[27] but they are also interesting on their own. Indeed, the physical properties of ultrathin polymer films differ considerably from those observed in the bulk, a phenomenon that requires a better understanding as the industrial uses of these films extend every day.[18,28]

From observations made on thin and ultrathin films using not only in-situ AFM but also optical microscopy,[29−34] transmission electron microscopy (TEM),[33−36] scanning electron microscopy (SEM),[37,38] and AFM of quenched samples,[30,31,33−39] several conclusions about the influence of film thickness on the crystallization process can be drawn. When the film thickness decreases, crystalline lamellae have a preferential orientation relative to the substrate which seems influenced by polymer−substrate interactions. For most of the systems investigated so far, lamellae are oriented flat-on to the substrate, i.e., with the polymer chain axis perpendicular to the substrate. The only polymers reported to have lamellae growing edge-on to the substrate when decreasing the film thickness down to thin and ultrathin dimensions are the poly(bisphenol A-*co*-alcanes), two model polymers extensively studied by the group of Chan,[6,7,9,10,20] and isotactic poly(propylene-*graft*-*tert*-butyl acrylate).[14] Thin films offer an opportunity to study in situ the formation of polymer

* To whom correspondence should be addressed. E-mail: re.prudhomme@umontreal.ca.

10.1021/ma0482359 CCC: $30.25
Published on Web 12/24/2004

single crystals, their morphology, growth rates, and melting, as this is of fundamental interest for the understanding of polymer crystallization.[40] However, single-crystal classical morphologies with regular crystallographic faces vanish if the film thickness decreases below a limit specific to each polymer. Then, typical diffusion-controlled growth morphologies are observed, like fractal seaweed, dendritic, and dense branching morphologies.[13,31,33,37−39]

Growth rates have also been found to be affected by the film thickness in ultrathin films, i.e., below 100 nm. Since the pioneer work of Frank et al.[28] on poly(di-*n*-hexylsilane), several authors reported a significant decrease with the film thickness.[14,17,18,29−33] For example, the group of Miyamoto[32,33] reported a linear decrease of the growth rate of iPS with the inverse of the film thickness, coming from a decrease in the mobility of the polymer chains. Schönherr et al.[14,17] observed an exponential dependence in the case of poly(ethylene oxide) (PEO); this behavior was explained by an increase of the glass transition temperature with a decrease of the film thickness, i.e., again a decrease in the mobility of the polymer chains.

In a previous work, we reported the influence of film thickness on the crystallization of thin and thick poly(ϵ-caprolactone) (PCL) and PCL/PVC blends films,[41] for film thicknesses ranging from 2000 to 100 nm. In that range, growth rates have been found to depend on film thickness for the blend but not for pure PCL. In this paper, the influence of film thickness on the morphology, growth rates, and melting of lamellar crystals grown in ultrathin films of pure PCL is investigated. Isothermal crystallization was followed by in-situ hot stage AFM at 50 and 54 °C for six film thicknesses ranging from 200 to 6 nm and at 30 °C for three film thicknesses ranging from 6 to 1 nm. Morphological and kinetic variations are discussed in terms of diffusion of the polymer chains from the melt to the growing crystal in ultrathin films.

Poly(ϵ-caprolactone) (PCL) was chosen for its unusual ability to be miscible with several polymers,[42] like poly(vinyl chloride) (PVC),[43,44] but also for its biodegradable properties which are required in the field of drug delivery[45] and of tissue engineering.[46] In addition, a low melting temperature, close to 60 °C like for PEO, but with much lower growth rates (around 500 times less at 46 °C for example),[30,41] makes PCL a convenient polymer for practical experimental reasons. Finally, PCL can be considered as an alternative model for the study of polymer crystallization, with a crystal structure very close to that of polyethylene,[47] the "model" semicrystalline polymer.

Experimental Section

Materials. Poly(ϵ-caprolactone) (PCL, $M_n = 39\,000$ and $M_w/M_n = 1.4$) was purchased from Aldrich Chemicals and used without further purification. Its molecular weight was determined by gel permeation chromatography. The glass transition temperature (T_g) and melting point of PCL were found to be −60 and 60 °C, respectively, using a Perkin-Elmer DSC-7 calorimeter at a heating rate of 20 °C/min. To prepare thin and ultrathin films, PCL was dissolved in tetrahydrofuran (THF) for at least 24 h, at room temperature and in the absence of light.

Sample Preparation. Thin and ultrathin PCL films were prepared by spin-coating solutions of PCL in THF with concentrations between 0.25 and 30.0 mg/mL (film thickness between 1 and 200 nm) onto cleaned Si substrates (p-type single-side polished (100) silicon wafers) using a Headway Research Inc., EC101 spin-coater at 3000 rpm for 20 s. Si substrates were cleaned by immersion in a sulfochromic acid solution for 2 min to remove any organic contamination and to hydroxylate the native oxide layer, thus making the surface hydrophilic[48] (sulfochromic acid should be handled and neutralized with care). Static contact angles measured with glycerol decreased from 33° for as-received substrates down to <5° after sulfochromic treatment. The substrates were then rinsed with Nanopure water and dried by spinning for 80 s at 3000 rpm just before spin-coating the PCL solution. To keep a solvent saturated atmosphere around the sample and to allow a uniform evaporation, a glass dome was placed on top of the sample area during spin-coating. Film thicknesses were measured by profilometry using AFM.[41]

Atomic Force Microscopy. A Nanoscope III Multimode AFM (Digital Instruments (DI), Santa Barbara, CA), operated in tapping mode and equipped with a high-temperature heater accessory (DI), was used to capture images at ambient conditions, without heating, and for in-situ observations of isothermal crystallizations at various temperatures. A J-scanner was used (maximum scan size 130 μm × 130 μm) with RTESP silicon probes (Nanoprobes). Temperature calibration of the hot stage was verified with both a thermocouple and a benzophenone sample of known melting point (48 °C). As the maximum film thickness (200 nm) investigated here is below the 500 nm limit found by Schönherr et al.[15] for PEO, it was assumed that the temperature of the sample was the temperature read on the hot-stage controller.

Spin-coated samples were cut with a diamond scriber down to a small square area which was glued with epoxy resin on a thin steel puck of 6 mm in diameter. Samples were first imaged at ambient conditions, i.e., at the temperature of the scanner, between 25 and 27 °C after warm-up, for observation before any thermal treatment. Then, the AFM probe was disengaged before the melting of the polymer film for 10 min at 100 °C. At this stage, the AFM probe was heated to the sample temperature to avoid any moisture and/or low molecular material condensation on the tip and cantilever (that harms the operation in tapping mode) but also to give a better temperature control of the sample surface examined by the probe and, finally, to avoid local melting or crystallization caused by a hotter or cooler tip; the sample and tip temperatures were then brought together to the desired temperature for isothermal crystallization, 50 or 54 °C for example, in about 1−2 min. Thermal stabilization was achieved for an additional 3 min before imaging, after tuning again the driving frequency of tapping (temperature dependent). Height, amplitude, and phase images were collected simultaneously. The scan rates varied from 0.3 to 2.5 Hz depending on the scanned image size (from 100 μm × 100 μm down to 500 nm × 500 nm), the free oscillation amplitude was set to 2.0 V, and the amplitude set point was between 1.3 and 1.6 V to track the surface without disturbing nucleation or crystal growth. Film thicknesses were measured at 60 °C on melted films (scratches were made with a sharp scalpel to remove part of the film before melting). Each sample was used only once, at one crystallization temperature.

Growth rates were measured on amplitude or phase images depending on which conditions gave the best contrast between the crystal and the surrounding melt. Images were recorded automatically one after the other with the "continuous" function of the Nanoscope software, but only half of them were used, either all those taken scanning upward or all those taken scanning down. Sequences of images were analyzed with the Image-Pro Plus 4.0 software, measuring for each image the distance between the center of the PCL crystal and the slow and fast growing directions; these directions are perpendicular and correspond to the two axes of symmetry of the crystal in the plane of the lamella. They also correspond to the crystallographic *a*- and *b*-axes.[16] Sequences of 10−30 images were used to follow the growth of PCL crystals. Growth rates in the slow and fast growing directions were obtained by plotting the respective distances from the center of the crystal as a function of time. The slopes of the straight lines obtained were determined leading to the slow and fast growth rates G_a and G_b, respectively.

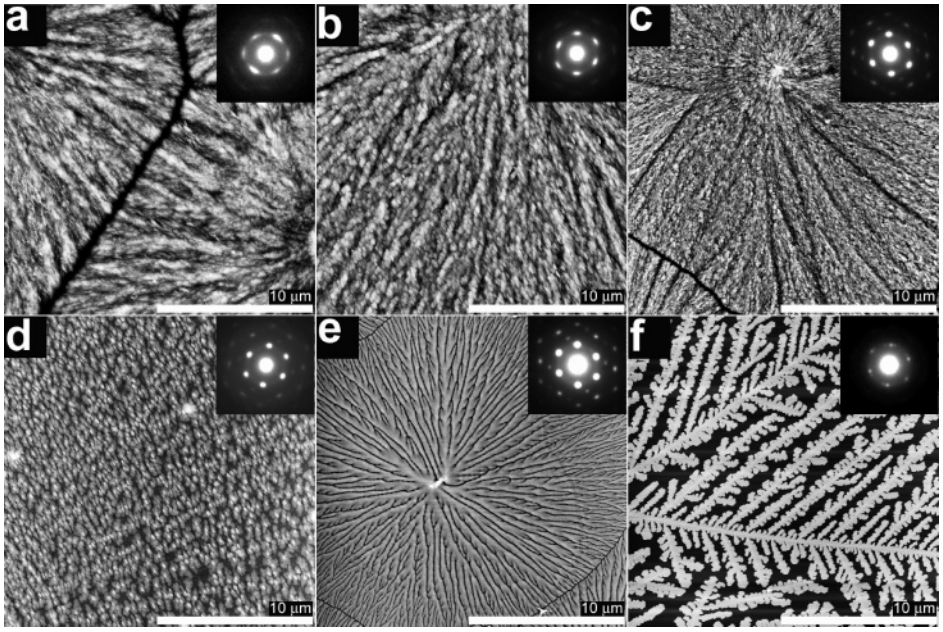

Figure 1. Tapping mode AFM height images (20 × 20 μm^2) of PCL films crystallized for 24 h at room temperature at film thicknesses of (a) 200, (b) 120, (c) 60, (d) 30, (e) 15, and (f) 6 nm, with corresponding selected-area electron diffraction patterns.

Transmission Electron Microscopy (TEM). A JEOL JEM-1230 TEM operating at 120 kV was used to observe, at room temperature, selected area electron diffraction patterns of crystallized samples. PCL samples for electron diffraction analysis were spin-coated on substrates which were prepared as follows: a 10 nm thick carbon film (thickness measured by AFM) was first evaporated on freshly cleaved mica, and then the hydrophobic carbon surface was turned hydrophilic[49] using a glow discharge in reduced air atmosphere, at 20 W for 10 s in a plasma cleaner (Harrick). Electron diffraction samples were spin-coated like AFM samples and crystallized at room temperature or melted for 10 min at 100 °C and isothermally crystallized in a Linkam hot stage. After crystallization, samples were quickly cooled to room temperature, and then the carbon film (covered by the polymer film) was detached from the mica substrate by floating in Nanopure water and transferred to a copper grid for electron diffraction observations.

Results and Discussion

Morphology: Crystallization at Room Temperature. AFM observations performed at room temperature 5 min after spin-coating indicated that out of the six PCL film thicknesses investigated, i.e., 200, 120, 60, 30, 15, and 6 nm, only the thinnest ones, 15 and 6 nm, are not fully crystallized.[50] However, after 24 h at room temperature, crystallization is completed in all cases, as shown in Figure 1, in which six AFM height images corresponding to the six film thicknesses studied were recorded. On each image, an electron diffraction pattern is added.

From these AFM height images, it is seen, first, that from thicknesses of 200 nm down to 60 nm (Figure 1a–c) there is a morphology that looks spherulitic with a radial centrosymmetric organization. However, the electron diffraction patterns contradict this conclusion since, as for the six film thicknesses exhibited in Figure 1, they indicate the presence of flat-on lamellae since all the diffraction spots correspond to the (hk0) projection of the reciprocal lattice of the structure of PCL;[47] therefore, the PCL chains are oriented normal to the substrate surface. The sharpness of the diffraction spots improves with the decrease of the film thickness, which indicates that the number of overgrowth lamellae with a different orientation decreases with the film thickness. This is illustrated by the higher resolution AFM height images available as Supporting Information S1 to S4, for corresponding film thicknesses of 200, 120, 60, and 30 nm. From these images, the flat-on orientation of most of the overgrowths can be observed, whereas some branched edge-on lamellae characteristic of the spherulitic morphology are observed in 200 and 120 nm films. This is consistent with the fuzziness of the diffraction spots in Figure 1a,b. At these film thicknesses, one goes from an axialitic morphology in the ultrathin films to a spherulitic morphology in the thicker films. It should be noted that the electron diffraction beam has a diameter of 3 μm, and electron diffraction patterns do not correspond to the full dimension of the crystal aggregates shown in Figure 1.

The size of the overgrowths decreases with the film thickness, as observed from Figure 1a–c and the corresponding Supporting Information. A decrease of the amount of polymer melt available could be responsible for the corresponding decrease of lateral dimensions. In Figure 1d, in a 30 nm PCL film, the overgrowths do not overlap due to a decrease of the polymer melt available. The radial organization is still present but less clearly observed, as the stacks of overgrowths are not continuous anymore. Electron diffraction demonstrates that the lamellae are flat-on and that the superposed lamellae have exactly the same crystallographic orientation, whatever their location in the image.

A further decrease of the film thickness down to 15 nm shows (Figure 1e) that there is only one layer of PCL lamella with a dendritic pattern, characteristic of diffusion-controlled growth. In Figure 1e, the width of the branches lies between 200 and 400 nm, excluding the possibility of having edge-on lamellae (when crystallized at 20 °C, the PCL lamellar thickness is below 10 nm), which is confirmed by the electron diffraction pattern characteristic of a flat-on lamella.

These observations recall the work of Taguchi et al.[33] on iPS, who correlated the occurrence of iPS lamellae growing flat-on (with a similar dendritic morphology) to a decrease of film thickness. In addition, they

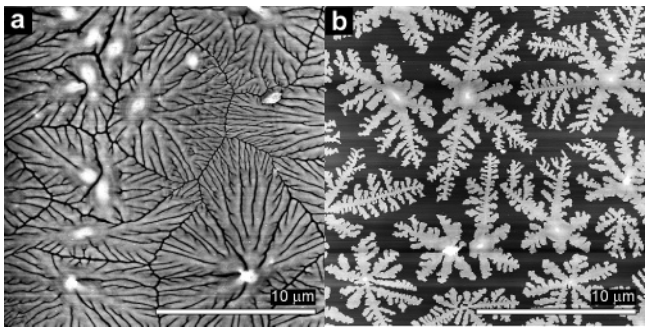

Figure 2. Tapping mode AFM height images of PCL films crystallized at room temperature on carbon-coated substrates at film thicknesses of (a) 15 and (b) 6 nm.

observed that the width of the branches increases with a decrease of the film thickness, which is also observed in Figure 1f for a 6 nm thick PCL film, with branches width between 300 and 700 nm, for an average thickness of 7−8 nm. At this film thickness, after crystallization, the polymer film does not cover all the substrate surface, although no dewetting, similar to that observed by Kressler et al.,[51] is observed here. The diffraction pattern confirms the flat-on orientation with, however, a decrease of the intensity of the diffraction spots with 110 and 200 reflections only, due to the lower amount of diffracting material as a consequence of the dendritic morphology.

Figure 2 illustrates the slightly different morphologies observed for PCL films obtained on carbon-coated substrates and used for electron diffraction. Parts a and b of Figure 2 are AFM height images of 15 and 6 nm films, respectively. As illustrated by these AFM images, the carbon-coated substrates give slightly different but comparable morphologies as those obtained on Si substrates and presented in Figure 1e,f. However, the dendrites grown on carbon-coated substrates have branches with larger widths, perhaps due to different polymer−substrate interactions.

Morphology: Crystallization at 54 °C. To the six samples imaged after crystallization at room temperature and shown in Figure 1a−f correspond Figure 3a−f for samples of matching thicknesses imaged "in situ" during isothermal crystallization at 54 °C. For the six film thicknesses, crystallization at 54 °C is not spherulitic. For thicknesses between 200 and 30 nm, lamellar crystals with a general shape reminiscent of flat-on PCL single crystals obtained from solution[52,53] are observed. Beekmans et al.[16] were the first to observe flat-on PCL lamellae with a truncated lozenge shape by in-situ AFM observations. Following the work of Brisse and Marchessault,[53] who observed PCL single crystals grown from solution, they concluded that PCL lamellar crystals grown from the melt exhibit four {110} and two {100} growth faces. The direction of the crystallographic *a*- and *b*-axes is shown by arrows in Figure 3a, with the *b*-axis in the direction of the larger growth. The exact orientation of the *a*- and *b*-axes and the confirmation of the crystallographic order in the lamellar crystals were obtained by electron diffraction.

In the six AFM images shown in Figure 3, the crystallized area is surrounded by amorphous melt. For all the thicknesses except 15 and 6 nm, spin-coated films crystallized at room temperature were first melted at 100 °C for 10 min before isothermal crystallization, as described in the Experimental Section of this paper. For the 15 and 6 nm films, this procedure leads to obvious dewetting. Indeed, at such low thicknesses, the crystallization process generates areas where the polymer layer becomes very thin between the branches as in Figure 1e or even thinner as illustrated by Figure 1f. To generate uniform melted films, the time between spin-coating and melting has to be as short as possible in order to limit the crystallization taking place before melting. Melting for more than 3 min or at a higher temperature than 90 °C leads to a dewetting of the 6 nm thick films.

For films thicknesses of 200 and 120 nm (Figure 3, a and b, respectively) amplitudes images are given instead of height images because for those thicknesses details of the lamellar structure were difficult to observe in height images due to the large height contrast between the growing crystal and the surrounding melt depletion area. In Figure 3a, between six and seven superposed lamellae can be estimated in a kind of poorly defined screw dislocation. The larger lamella and at least the two following ones, when going up in the *c* direction, have well-defined faces and angles, with a truncated lozenge shape and a certain curvature of the {100} growth faces. Some disorder along the *b* direction can be noted; it comes from additional nucleation in this area, leading to a buildup of lamellae. As very high forces were applied to the AFM tip to capture Figure 3a, no large depletion of the melt can be observed at the crystal−melt interface. In Figure 3b, a large number of overgrowth lamellae are also observed, giving an irregular topography to the crystal which maintains the same hexagonal outer shape.

In parts c and d of Figure 3, for films thicknesses of 60 and 30 nm, respectively, only one basal lamella exhibits the full truncated lozenge shape. Overgrowth lamellae are observed with orientations similar to the basal lamella, but they are not fully developed due to a lack of available melt. They are nucleated by substrate defects, not by screw dislocations, and their size and number decrease with the film thickness. Overgrowths are nearly always present in the crystal center, nucleated by the major defect that gave birth to the basal lamella. Basal lamellae without any overgrowth were observed in a few occasions in 60 and 30 nm thick films, presumably when the heterogeneous nucleus was too small to give birth to overgrowth lamellae. In Figure 3d, overgrowths are rare, and a maximum of three layers of lamellae are superposed. Careful observations of the contrast at the overgrowth boundaries, and the occurrence of overgrowth lamellae that amalgamate when meeting whereas other overlap, lead us to the conclusion that part of the overgrowths are nucleated below the basal lamella, whereas others are nucleated above. This phenomenon has already been described by Kikkawa et al.[54] for poly(L-lactide) (PLLA) thin films, using enzymatic degradation. More details are given below, and the phenomenon is better illustrated in Figure 5.

The basal lamella observed in Figure 3d can be divided into six sectors, with three prominent lines corresponding to the sector boundaries. We assume that the six sectors correspond to areas of identical dominant fold orientation, with chain folding direction parallel to the growth face in the four {110} sectors and, alternatively, in the [110] and [1−10] directions for the two {100} sectors,[55] as proposed for polyethylene. Striations roughly perpendicular to the growth faces are observed in the six thicknesses investigated, although they are

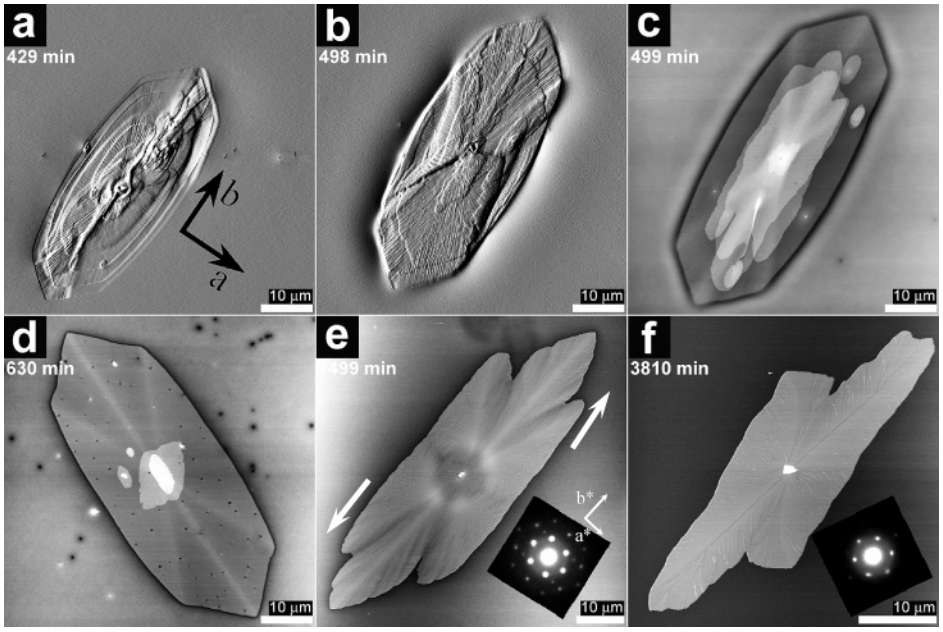

Figure 3. Tapping mode AFM images of PCL films isothermally crystallized at 54 °C at film thicknesses of (a) 200, (b) 120, (c) 60, (d) 30, (e) 15, and (f) 6 nm. (a) and (b) are amplitude images, and the others are height images. The corresponding electron diffraction patterns are added in (e) and (f). The time interval between nucleation and capture of the AFM image is given on each image.

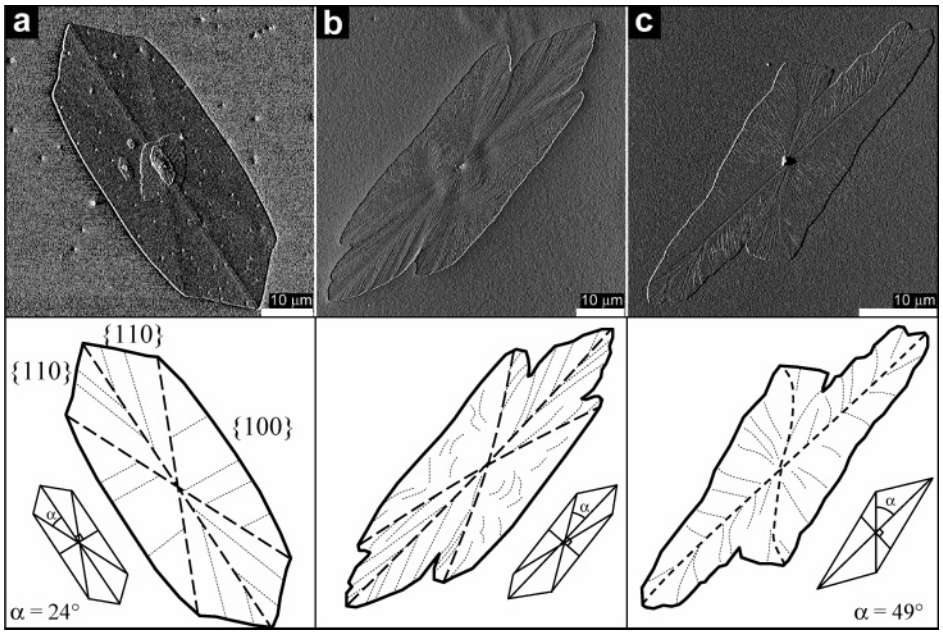

Figure 4. Tapping mode AFM amplitude images of PCL films isothermally crystallized at 54 °C at film thicknesses of (a) 30, (b) 15, and (c) 6 nm; they correspond to parts d, e, and f of Figure 3, respectively. A schematic representation of the lamellar crystals is sketched below each AFM image. Boundaries of the sectors (large dashed lines), representative striations observed in each sectors (dotted lines), and a reduced representation of the geometric shape of the lamellar crystal are indicated with the α angle. In (a), positions of the {110} and {100} sectors are also shown.

hardly distinguishable in the height images presented in Figure 3. This phenomenon has recently been described by Taguchi et al.[36] as resulting from surface stresses. Their evolution as a function of film thickness is described later in this paper, and illustrated in Figure 4, as well as in the enlarged images S5, S6, and S7 of the Supporting Information.

When the film thickness decreases down to 15 nm, PCL lamellar crystals do not exhibit overgrowth anymore and are only composed of the basal lamella, as observed in Figure 3e. Electron diffraction confirms the orientation of the *a*- and *b*-axes relative to the lamellar crystal, given in Figure 3a, and indicates a high crystallographic order. However, the hexagonal shape of the lamellar crystal is distorted, as if a shear force would have been applied to the lamella, as illustrated in the AFM image by the two white arrows. For lamellar crystals longer than 10−20 μm, a rupture of the four {110} growth faces is observed. The shape and size of the striations observed in the {100} sectors are more irregular than those observed in the four {110} sectors, as described in Figure 4 (see image S6 of the Supporting Information). The circular depression observed at the center of the crystal is not a morphological feature characteristic of this film thickness, but a defect of the melted film that does not affect the morphology or the

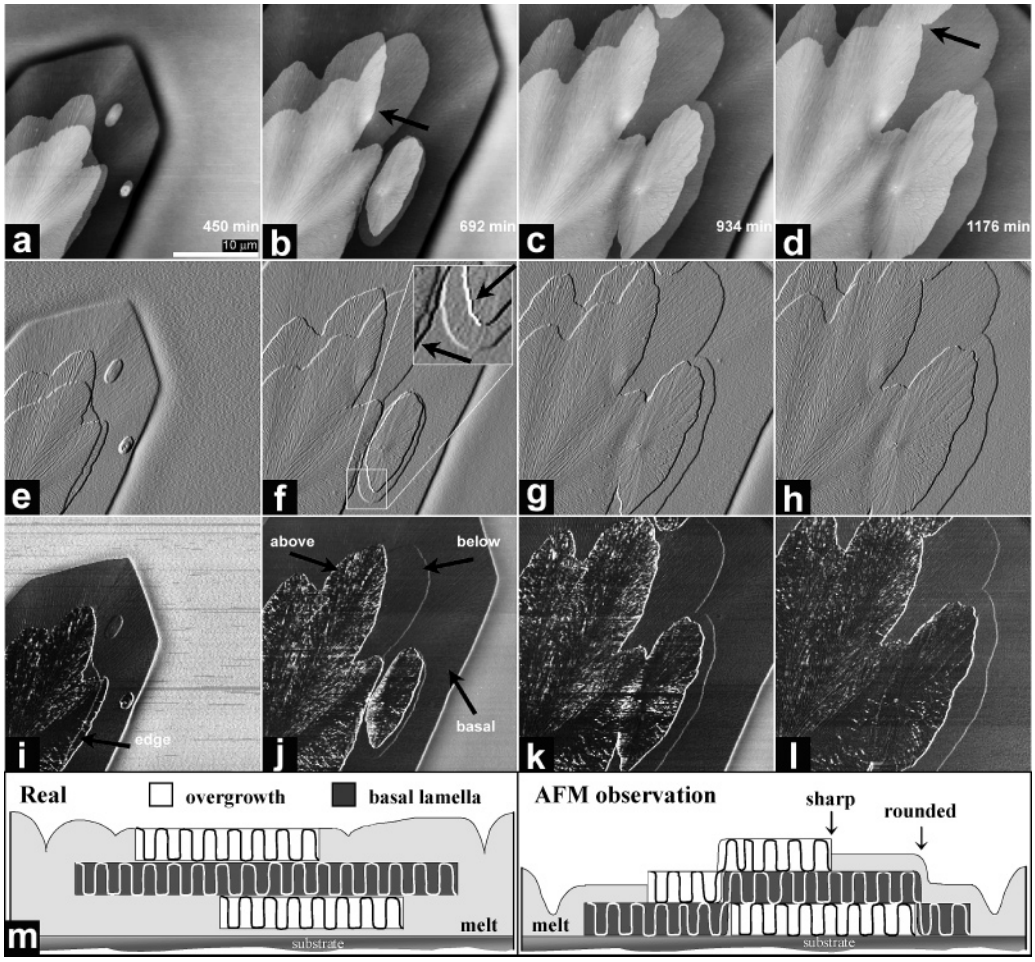

Figure 5. Tapping mode AFM images (30 × 30 μm^2) of a 60 nm thick PCL film isothermally crystallized at 54 °C (enlargement of the upper-right area of the original (60 × 60 μm^2) image sequence from which Figure 3c was taken): (a, b, c, d) height images; (e, f, g, h) amplitude images; (i, j, k, l) phase images. The time interval between nucleation and capture of the AFM images is given on each height image. In (f), the magnification of the area indicated by a white square is shown. Black arrows drawn on some images indicate areas of interest (see text). In (m), two schematic diagrams illustrate the difference between the real morphology and the morphology felt by the AFM tip due to the possible bending of the lamellar crystals under the pressure of the tip.

growth kinetics of the crystal. The distortion of the hexagonal shape of the lamellar crystal increases when the film thickness decreases further, as observed in Figure 3f for a 6 nm thick film, for which the outline of the crystal could be better represented by a parallelogram than a hexagon. The corresponding electron diffraction pattern indicates a lower crystallographic order in comparison with the lamellar crystals obtained in the 15 nm thick films. A rupture line similar to that observed in the four {110} growth faces of Figure 3e, and developing only in lamellar crystals longer than 10−20 μm, is now observed on the two small faces of the parallelogram, the two large faces being almost straight. This morphological evolution mimics the disappearance of two of the originally four {110} sectors. It should be noticed that the distortions (shear) and disappearance of {110} sectors were observed both as illustrated in Figure 3 and in a mirror symmetry, namely modifying the {110} sectors on the lower right and upper left side of the *b*-axis, and this with the same occurrence.

The thickness of the basal lamellae in 60, 30, 15, and 6 nm thick films has been measured to be about 10−13 nm in all films crystallized at 54 °C (AFM measurements were impossible in 200 and 120 nm thick films). This is an approximate value since the lamellar thickness is difficult to determine by AFM due to the presence of the melt surrounding the growing crystal, but it was measured as the height difference between the crystal surface and the bottom of the surrounding depletion area for 15 and 6 nm films where no overgrowth is observed and between the overgrowth and the basal lamella surface for 60 and 30 nm films. In addition, as the tip−sample force interactions are different between the crystalline lamella and the surrounding melt, as observed in phase images, the melt is probably seen more elevated than it is in reality, which makes the thickness measurements semiquantitative.

In 6 nm thick films, the lamellar crystal is about 2 times thicker than the melted layer, and the polymer chains need to diffuse from a larger distance to reach the lamellar growth front as compared to thicker films. Distortion of the lamellar crystal is thus logically observed in films of similar thickness or thinner than the lamellar thickness, i.e., 10−13 nm at 54 °C.

The morphological evolution with the film thickness is schematically illustrated in Figure 4, in which amplitude images, corresponding to the height images of Figure 3d−f, are depicted. In the three cases, the outline of the lamellar crystals is drawn in addition to the sector boundaries (large dashed lines) and representative striations observed in each sectors (dotted

lines). A reduced representation of the geometric shape of the lamellar crystal is also drawn, in which the α angle is indicated. This angle is almost constant (24°) for film thicknesses between 200 and 15 nm and significantly increases (49°) with the distortion of the lamellar crystal for 6 nm films.

It must be noticed that, in the 15 and 6 nm thick films, both the hexagon/parallelogram transition and the rupture of the {110} sectors develop during the growth of the lamellar crystals. They are certainly driven by a decrease of the available melt layer around the lamellar crystal and, subsequently, a slower diffusion of the polymer chains to the growth front.

The striations observed in each sector of the lamellar crystals are difficult to observe in details in the AFM images of Figure 4, but representative striations are indicated in dotted lines in the schematic diagrams. In Figure 4a, for a 30 nm thick film, the striations are very regular and nearly perfectly parallel in each sector. In the {100} sectors, the striations are perpendicular to the growth front, whereas in the {110} sectors, they make an angle with the *b*-axis close to the α angle, which is about 24°. In other words, the striations found in the {110} sectors are nearly parallel to the boundary line of this sector with the {100} sector, but they are not perpendicular to the growth front.

When the film thickness decreases to 15 nm, as observed in Figure 4b, the striations of the {100} sector become very irregular, and they are not anymore perpendicular to the {100} growth faces. Striations observed in the now disrupted {110} sector are bent in the direction of the rupture line. This appears to be the result of the progressive change of their orientation since this orientation was first similar to that observed for thicker films before the rupture of the growth front, but progressively, it changed, presumably to keep the same angle with the growth front. In Figure 4c, when the film thickness further decreases to 6 nm, it becomes difficult to determine accurately the position of the different sectors, but the bending of the striations becomes more important, especially close to the rupture of the two disrupted growth fronts (presumably in the two {110} sectors). The progressive modification of the growth front orientation seems again to be responsible for this phenomenon. The more irregular striations observed when the film thickness decreases seem to be related to a poorer organization of the lamella. This point will be discussed later in this paper in relation with the melting of lamellar crystals.

Overgrowth Above and Below the Basal Lamella. In-situ observations of growing overgrowths lead to the conclusion that some of them nucleate above the basal lamella, whereas others nucleate below. This phenomenon is described in details in Figure 5 by a series of AFM images extracted from the same sequence in which Figure 3c was taken, the 12 images having the same lateral dimensions. The complete sequence of AFM images is available as Supporting Information S8. Four different times of crystallization are captured in Figure 5, and for each of them, height (a, b, c, and d), amplitude (e, f, g, and h) and phase images (i, j, k, and l) are depicted. From the height images, four different height levels can be observed, corresponding to the melt (around the growing basal lamella), the basal lamella, the basal lamella with one overgrowth layer, and the basal lamella with two overgrowth layers. In the height images, overgrowth lamellae are sometimes seen to overlap and, at other times, to amalgamate when meeting. Two clear examples of amalgamations are indicated by the black arrows of Figure 5b,d.

This observation leads to the suggestion that lamellae that overlap are not growing on the same side of the basal lamella, whereas lamellae that amalgamate grow together either above or below the basal lamella. This hypothesis is confirmed by the phase images, in which part of the overgrowth lamellae exhibit a phase shift as compared to the basal lamella. The phase shift observed by AFM can result from a difference of viscoelasticity of the sample, a difference in the adhesion forces felt by the probe, or even from topographic variations. Here, we assume that the overgrowth lamellae that nucleate above the basal lamella are covered by a thinner layer of melt or even by no melt at all. This absence of melt layer, or decrease of its thickness on top of the crystalline lamellae, should be responsible for the phase shift detected by the AFM probe, as the melt layer is soft compared to the crystalline lamella and certainly somehow sticky. In contrast, no phase shift is observed between the basal lamella alone and the basal lamella with an overgrowth lamella nucleated below, as the presence of the overgrowth does not affect the thickness of the melt layer above the basal lamella. In Figure 5j, three arrows indicate the position of the basal lamella and of the overgrowths nucleated above and below.

It is also interesting to notice that in the phase images an overgrowth nucleated below the basal lamella is difficult to observe "through" an overgrowth nucleated above, contrary to the observations in the height images, which confirms that the contrast in phase images does not come from topographic variations. One exception, however, is indicated by an arrow in Figure 5i.

The observation of overgrowth lamellae nucleated below the basal lamella indicates that the basal lamella is soft enough to bend under the pressure of the AFM tip. This should not be surprising considering the very small thickness of the lamellae as compared to their lateral dimensions. Indeed, AFM images can be misleading if the lateral dimensions (micrometers), which are about a thousand times larger than the vertical dimension (nanometers), are not considered.

In the amplitude images, a difference of sharpness is observed between the boundaries of the overgrowth nucleated above and below the basal lamella. As illustrated in Figure 5f with an enlargement of a selected area, overgrowths, likely nucleating above the basal lamella from the phase image analysis, exhibit boundaries with a higher contrast (indicated by two arrows) than overgrowths nucleating below the basal lamella. In amplitude images, this observation implies a sharper change of the topography since the overgrowth below the basal lamella is felt by the AFM probe through the crystalline layer of the basal lamella, which makes the accurate observation of the details of the edges impossible (as a carpet would prohibit the proper observation of the edges of a book that would lay below). A schematic diagram, representing the phenomenon described above, is shown in Figure 5m: on the left-hand side is shown a representation of the assumed real morphology of a film with a basal lamella and overgrowths growing above and below and on the right-hand side, the topography felt by the AFM probe. This model is consistent with that proposed by Kikkawa et al.[54]

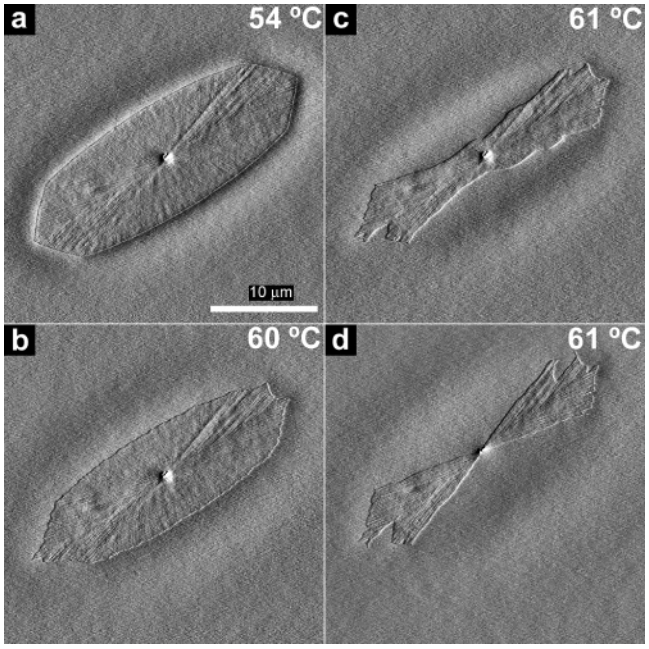

Figure 6. Tapping mode AFM amplitude images (30 × 30 μm^2) of the melting of a lamellar crystal isothermally crystallized at 54 °C in a 60 nm thick PCL film: at (a) 54, (b) 60, (c) 61, and (d) 61 °C, 32 min later than (c).

Melting of Crystallized Films. First, the melting of a lamellar crystal grown at 54 °C in a 60 nm thick film is illustrated in Figure 6 by four AFM amplitude images; a lamellar crystal without overgrowth has been chosen as it enables a better observation of the melting phenomenon, even if such isolated basal lamellae are rare in 60 nm thick samples. Overgrowths melt at lower temperatures than the basal lamellae due to a poorer crystalline organization resulting from their development in a constrained environment on top or below the basal lamella, with a lower supply of melt as compared to the basal lamellae. When overgrowths are present, the basal lamella can start to melt preferentially at the points of contact with melted overgrowths, which modifies the melting process. However, it is unclear whether this preferential melting occurs due to the presence of the melted overgrowths or due to substrate defects from which overgrowths nucleate. This phenomenon is illustrated by Supporting Information S9, an animation of AFM height images, showing the growth at 54 °C, and ulterior melting, in a 30 nm film.

In Figure 6a is shown an image taken at 54 °C, just before melting the sample. In Figure 6b, taken at 60 °C, the crystal has begun melting, the free edges first, i.e., the polymer chains which crystallized the last; at that temperature, the crystal still maintains its original shape, as in Figure 6a. If the sample is kept at 60 °C for a certain period of time (not illustrated in Figure 6), the edges stop melting, which indicates that the crystal is not homogeneous, maybe due to the longer annealing time experienced during the crystallization in the inner area of the crystal as compared to the edges. Moreover, the crystalline polymer chains found at the edges of the crystal and, therefore, in contact with the melt can melt easily due to a larger mobility in comparison with the polymer chains found in the rest of the crystal, which are surrounded by other crystallized polymer chains. This preferential melting of the edges can lead to a preferential recrystallization, which will finally protect the rest of the crystal from melting if the temperature is held constant. Traces of such a recrystallization are observed in Figure 7d. In Figure 6c, the temperature is raised to 61 °C, leading to an asymmetric melting of the lamellar crystal: the two {100} sectors melt preferentially to such an extent that they are fully melted in Figure 6d, taken about 32 min later, whereas the four {110} sectors are still easily recognized. Complete melting of the lamellar crystal is observed at slightly higher temperature (about 1 °C) but is not illustrated here.

A comparable phenomenon has been observed for single crystals of linear polyethylene (LPE) grown from solutions[56] and for PLLA lamellar crystals grown from the melt.[54] These two polymers, like PCL, have an orthorhombic unit cell, and the lamellar crystals observed are truncated lozenges with two {100} and four {110} sectors. In both cases, the lower melting point of the {100} sectors has been interpreted in terms of a different chain folding organization.[55] In the {110} sectors, the chain folding direction is parallel to the growth front whereas, in the {100} sectors, the chain folding direction alternates between [110] and [1−10] directions, giving therefore a less stable organization and thus a lower melting temperature. From our observations, it is suggested that PCL single crystals behave like LPE and PLLA single crystals. Hocquet et al.[56] also found {110} sectors to be slightly thicker than {100} sectors due to a different tilt angle of the chains in the two sectors. No consistent thickness differences were found between the different sectors in the lamellar crystals of PCL observed during this study.

In Figure 7, the melting behavior of lamellar crystals grown at 54 °C in 30, 15, and 6 nm thick films is illustrated. For each thickness, an AFM phase image of the lamellar crystal taken at 54 °C, just before the melting, is shown above another AFM phase image taken during the melting at the temperature indicated on the image. In Figure 7a,b, a lamellar crystal grown in a 30 nm thick film exhibits a melting behavior close to that observed in the 60 nm thick film of Figure 6, with the two {100} sectors almost completely melted, whereas the four {110} sectors have just started to melt. In Figure 7c,d, for a lamellar crystal grown in a 15 nm thick film, the melting becomes more irregular with parts of the {110} sectors melting simultaneously with the {100} sectors. The melted areas of the {110} sectors correspond to the bent striations described previously in Figure 4, therefore corresponding to a poorer organization in the lamellar crystal. In addition, six branches, corresponding to the boundaries of the four {110} sectors, are still not melted in Figure 7d, indicating that parts of the {110} sectors still possess a better organization than the {100} sectors. Finally, in Figure 7e,f, the melting of a lamellar crystal grown in a 6 nm thick film indicates that, for such a low thickness, the different sectors melt at the same temperature, the melting pattern being irregular, without significant symmetries.

From Figures 6 and 7, the melting behavior of the PCL lamellar crystals crystallized at 54 °C is consistent with the morphological observations that indicated a poorer crystalline organization when the film thickness decreases, associated with a diffusion-controlled growth. It should be noted that the recorded melting temperatures depend on the heating rate chosen and, for each sample, the melting history was different, depending on the size of the scanned area and the time it took to record an image. Therefore, the information obtained

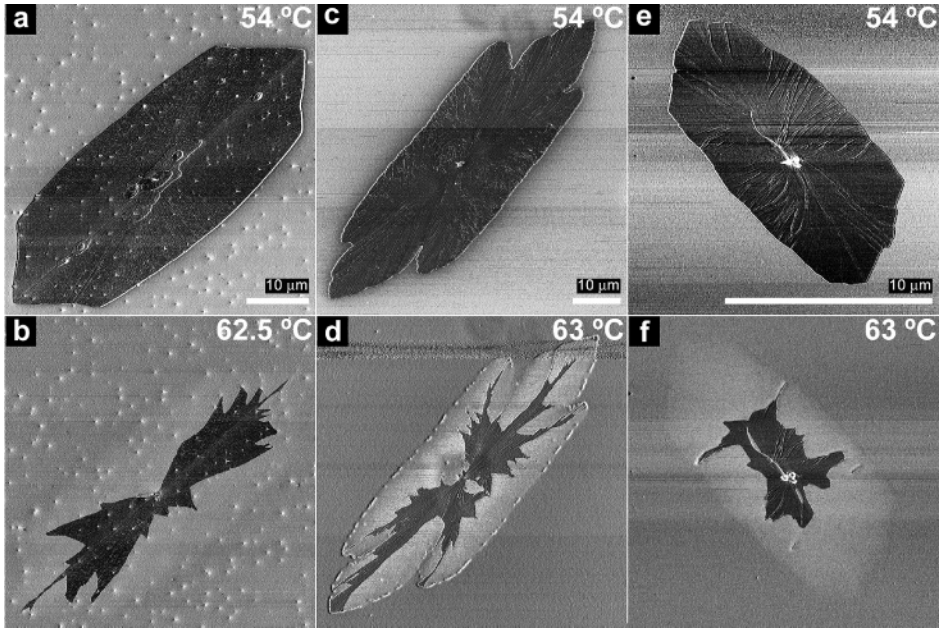

Figure 7. Tapping mode AFM phase images of the melting of lamellar crystals isothermally crystallized at 54 °C at three different film thicknesses: (a) 30 nm at 54 °C; (b) 30 nm at 62.5 °C; (c) 15 nm at 54 °C; (d) 15 nm at 63 °C, (e) 6 nm at 54 °C; (f) 6 nm at 63 °C.

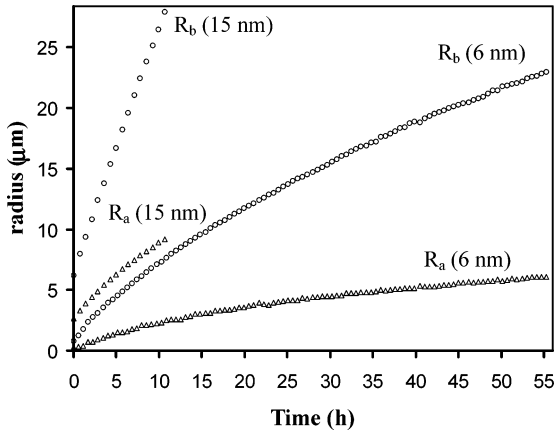

Figure 8. Lamellar crystal radius in the a and b directions (R_a and R_b) of samples isothermally crystallized at 54 °C at film thicknesses of 15 and 6 nm.

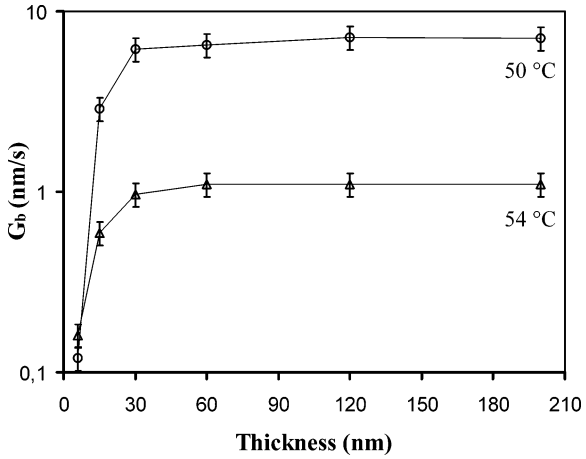

Figure 9. Radial growth rate of PCL films isothermally crystallized at 50 and 54 °C as a function of the film thickness in a semilogarithmic scale.

from these experiments is semiquantitative, and the melting temperatures given in this paper should not be compared one with another. In Figure 7d,f, the melted area corresponding to the location of the original crystal appears brighter than the rest of the film due to the phase contrast between the very thin melt layer surrounding the crystal and the thicker melt layer of the melted crystal. A phase contrast is observed as the AFM tip does not feel similarly the substrate through these two melt layers of different thicknesses.

Kinetics: Isothermal Crystallization at 54, 50, and 30 °C. In-situ AFM experiments allowed to follow the radial growth rate of lamellar crystals in the a and b directions, G_a and G_b. At 50 and 54 °C, the growth has been observed to be linear at all film thicknesses, except at 15 and 6 nm. The nonlinearity observed for 15 and 6 nm films crystallized at 54 °C, which becomes obvious only when the crystallization process is followed for a sufficiently long period of time, is illustrated in Figure 8, in which the growth in the b direction is roughly linear for the 15 nm thick film but not in the a direction, whereas for 6 nm thick films, the nonlinearity is observed in both the a and b directions.

To characterize the growth rates observed in 6 nm thick films, the slopes were calculated at the beginning of the nonlinear curves, arbitrarily fixed to the first 5 h of growth, corresponding to the maximum growth rate experienced by the lamellar crystal. The calculated growth rates G_b are plotted in Figure 9 as a function of film thickness for films crystallized at 50 and 54 °C. Error bars of 15% are shown illustrating fluctuations of the growth rate in successive experiments, originating from uncertainties in the film thickness and crystallization temperature. Figure 9 illustrates the decrease of the growth rate with the film thickness: G_b is constant for thicknesses between 200 and 30 nm at both temperatures and in good agreement with measurements obtained by optical microscopy in thicker films, up to 2000 nm,[41] corresponding to bulk growth rates. For 15 nm thick films, the growth rate is approximately half the bulk growth rate at both temperatures, whereas for 6 nm thick films, the growth rates are divided

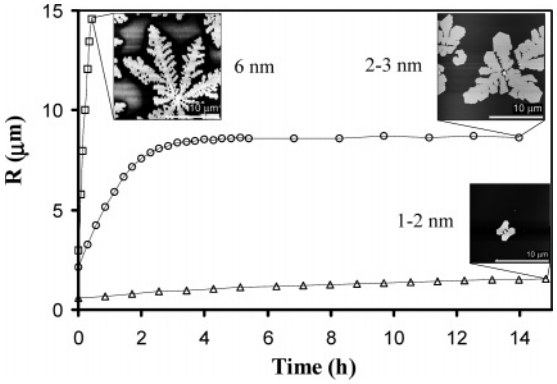

Figure 10. Dendritic crystal size of samples isothermally crystallized at 30 °C at film thicknesses of 6, 2−3, and 1−2 nm. The tapping mode AFM height images correspond to the last data point of each curve.

approximately by 7 and 54 as compared to the bulk values at 50 and 54 °C, respectively. Therefore, in 6 nm thick films, lamellar crystals grow approximately at the same rate at 50 or 54 °C. The morphological distortions of the lamellar crystals, the nonlinearity of the radial growth, and the growth rate decrease are all observed at the same film thicknesses, 6 and 15 nm, in which the diffusion of the polymer chains is the limiting factor. These thicknesses are equal to or below the lamellar thickness of about 10−13 nm at 54 °C and of about 9−11 nm at 50 °C. Reiter and Vidal[57] have already suggested that the thickness of the lamellar crystals of poly(styrene-*b*-ethylene oxide) copolymer thin films can be understood as the limiting thickness for the melted polymer films below which the crystal growth rate decreases due to the longer time needed to transport the polymer chains to the crystal growth front. An estimation of the radius of gyration of the PCL chains[58] gives a value of 7 nm. It should therefore be noted that the thicknesses studied here are of the same order of magnitude as the radius of gyration of the PCL chains.

For the crystallization of films thinner than 6 nm, the crystallization temperature was chosen below 50 or 54 °C to avoid too long experiments. Therefore, 2−3 and 1−2 nm thick films were crystallized at 30 °C, just after spin-coating, without heating the sample above the melting temperature of the PCL to avoid dewetting. (A range of thicknesses are reported due to the large uncertainty in their measurements.) In Figure 10, the radial dimensions of the dendrites observed in 6, 2−3, and 1−2 nm thick films crystallized at 30 °C are shown along with the AFM height images corresponding to the last data point of each curve. The decrease of the growth rate with the film thickness is obvious, affecting both the shape of the curves and the size of the dendrites observed in the AFM images. For a semiquantitative estimation, the slope of the quasi-linear section found at the beginning of each curve was calculated, which corresponds to the maximal growth rate experienced by the lamellar crystals. In 2−3 nm thick films, dendrites were found to grow about 10 times slower than in 6 nm thick films and about 275 times slower in 1−2 nm thick films. In the 2−3 nm thick films, the growth is observed to stop after 3−4 h when dendrite branches are still very distant one from another due to the lack of available amorphous polymer. In 1−2 nm thick films, the growth was observed to stop after a radial growth of 2−3 μm. For the three film thicknesses shown in Figure 10, the lamellar crystals are about 7 nm thick, independent of the film thickness. This phenomenon confirms the independence of the lamellar crystal thickness upon the film thickness, as already observed at 50 and 54 °C.

Therefore, at the crystallization temperatures and film thicknesses investigated, the thickness of the PCL lamellae, crystallized from the melt, depends only on the crystallization temperature, as predicted by theory: the higher the crystallization temperature, the thicker the lamella. When the melted film in which the lamella grows is thinner than the more favored lamella, the distance for polymer chains diffusion to the growth front becomes larger as the lamella grows; this is the origin of the nonlinear growth observed in this study in 15, 6, 2−3, and 1−2 nm ultrathin films, since the more the lamella grows, the thinner becomes the melted film surrounding the lamella. This is true up to the point when the melted film becomes so thin that no diffusion is possible anymore, which stops the growth of the lamella and leaves a very thin adsorbed layer of polymer melt on the substrate. This very thin polymer layer was observed by AFM after inducing its dewetting by heating the sample, which turns it into isolated droplets. The decrease of the melt thickness induced by the "pumping" of the melt by the growing crystals was also observed through the variation of the nonlinear growth with the number of growing crystals sharing the same area. Indeed, when nonlinear growth was observed, the growth of isolated crystals was faster than that of crystals surrounded by several other crystals also "pumping" the available melt, a phenomenon not observed in thicker films in which enough melt is available for every lamella (which grows linearly).

Conclusions

In summary, PCL ultrathin films (200−1 nm) have been found to crystallize with lamellae oriented flat on, even when crystallized at room temperature, in which case morphologies are dendritic for the thinner films (15 nm and below) and are flat-on axialites, i.e., stacks of flat-on lamellae with the same crystallographic orientation, covered by many overgrowths for the thicker ones (30 nm and thicker), with some branched edge-on lamellae observed in 120 and 200 nm films, indicating a shift to the spherulitic morphology. When crystallized at low undercooling, PCL crystals have a truncated lozenge shape, with overgrowths nucleated above or below the basal lamella when melted polymer is available (in films 30 nm and thicker). The morphology of those lamellar crystals is distorted in the thinnest samples (15 nm and below), with a rupture of the {110} sectors and a transition from a hexagonal to a parallelogram shape. The distorted lamellae do not show preferential melting in any of the sectors, contrary to undistorted lamellae in which {100} sectors have a lower melting temperature than {110} sectors. However, the lamellar thickness is not influenced by the film thickness, but only by the crystallization temperature.

Those morphological changes have been correlated with the nonlinearity of the growth and a decrease of the growth rate with the film thickness. The maximum growth rates (i.e., at the very beginning of the growth) experienced by the crystals growing in the thinnest films are 1 or 2 orders of magnitude smaller than those observed in the bulk at the same crystallization temperature.

As these phenomena have been observed for film thicknesses equal to or smaller than the lamellar

thickness, they can be explained by the reduced diffusion of the polymer chains from the melt to the growing crystal in constrained geometry. Indeed, in films thinner than the lamellar crystal, as the growth proceeds, diffusion of the polymer chains slows down due to a depletion area surrounding the crystal, which explains both the nonlinearity observed for the growth and the growth rate decrease.

Acknowledgment. This study was supported by NSERC and FCAR grants. We also acknowledge Professor J. Brisson for her help with electron diffraction and Ms. V. Landry for the contact angle measurements.

Supporting Information Available: Tapping mode AFM images of PCL films and QuickTime movies of tapping mode AFM amplitude and height images of PCL films. This material is available free of charge via the Internet at http://pubs.acs.org.

References and Notes

(1) Pearce, R.; Vansco, G. J. *Macromolecules* **1997**, *30*, 5843.
(2) Pearce, R.; Vansco, G. J. *Polymer* **1998**, *39*, 1237.
(3) Pearce, R.; Vancso, G. J. *J. Polym. Sci., Part B: Polym. Phys.* **1998**, *36*, 2643.
(4) Schultz, J. M.; Miles, M. J. *J. Polym. Sci., Part B: Polym. Phys.* **1998**, *36*, 2311.
(5) McMaster, T. J.; Hobbs, J. K.; Barham, P. J.; Miles, M. J. *Probe Microsc.* **1997**, *1*, 43.
(6) Li, L.; Chan, C.-M.; Yeung, K. L.; Li, J.-X.; Ng, K.-M.; Lei, Y. *Macromolecules* **2001**, *34*, 316.
(7) Li, L.; Chan, C.-M.; Li, J.-X.; Ng, K.-M.; Yeung, K.-L.; Weng, L.-T. *Macromolecules* **1999**, *32*, 8240.
(8) Hobbs, J. K.; McMaster, J. T.; Miles, M. J.; Barham, P. J. *Polymer* **1998**, *39*, 2437.
(9) Lei, Y.-G.; Chan, C.-M.; Li, J.-X.; Ng, K.-M.; Wang, Y. *Macromolecules* **2002**, *35*, 6751.
(10) Lei, Y.-G.; Chan, C.-M.; Wang, Y.; Ng, K.-M.; Jiang, Y.; Lin, L. *Polymer* **2003**, *44*, 4673.
(11) Beekmans, L. G. M.; Vallée, R.; Vancso, G. J. *Macromolecules* **2002**, *35*, 9383.
(12) Zhou, W.; Cheng, S. Z. D.; Putthanarat, S.; Eby, R. K.; Reneker, D.; Lotz, B.; Magonov, S.; Hsieh, E. T.; Geerts, R. G.; Palackal, S. J.; Hawley, G. R.; Welch, M. B. *Macromolecules* **2000**, *33*, 6861.
(13) Kikkawa, Y.; Abe, H.; Iwata, T.; Inoue, Y.; Doi, Y. *Biomacromolecules* **2001**, *2*, 940.
(14) Schönherr, H.; Waymouth, R. M.; Hawker, C. J.; Frank, C. W. *Polym. Mater. Sci. Eng.* **2001**, *84*, 453.
(15) Schönherr, H.; Bailey, L. E.; Frank, C. W. *Langmuir* **2002**, *18*, 490.
(16) Beekmans, L. G. M.; Vancso, G. J. *Polymer* **2000**, *41*, 8975.
(17) Schönherr, H.; Frank, C. W. *Macromolecules* **2003**, *36*, 1199.
(18) Schönherr, H.; Frank, C. W. *Macromolecules* **2003**, *36*, 1188 and cited references.
(19) Schönherr, H.; Waymouth, R. M.; Frank, C. W. *Macromolecules* **2003**, *36*, 2412.
(20) Jiang, Y.; Yan, D.-D.; Gao, X.; Han, C. C.; Jin, X.-G.; Li, L.; Wang, Y.; Chan, C.-M. *Macromolecules* **2003**, *36*, 3652.
(21) Ivanov, D. A.; Amalou, Z.; Magonov, S. N. *Macromolecules* **2001**, *34*, 8944.
(22) Godovsky, Y. K.; Magonov, S. N. *Langmuir* **2000**, *16*, 3549.
(23) Basire, C.; Ivanov, D. A. *Phys. Rev. Lett.* **2000**, *85*, 5587.
(24) Hobbs, J. K.; Humphris, A. D. L.; Miles, M. J. *Macromolecules* **2001**, *34*, 5508.
(25) Kikkawa, Y.; Abe, H.; Fujita, M.; Iwata, T.; Inoue, Y.; Doi, Y. *Macromol. Chem. Phys.* **2003**, *204*, 1822.
(26) Hoffman, J. D.; Davis, G. T.; Lauritzen, J. I., Jr. In *Treatise in Solid State Chemistry*; Hannay, N. B., Ed.; Plenum: New York, 1976; Vol. 3, pp 497−614.
(27) Mareau, V. H.; Prud'homme, R. E. In *Soft Materials: Structure and Dynamics*; Dutcher, J. R., Marangoni, A., Eds.; Marcel Dekker: New York, 2004; Chapter 2, pp 39−71.
(28) Frank, C. W.; Rao, V.; Despotopoulou, M. M.; Pease, R. F. W.; Hinsberg, W. D.; Miller, R. D.; Rabolt, J. F. *Science* **1996**, *273*, 912 and cited references.
(29) Dalnoki-Veress, K.; Forrest, J. A.; Massa, M. V.; Pratt, A.; Williams, A. *J. Polym. Sci., Part B: Polym. Phys.* **2001**, *39*, 2615.
(30) Massa, M. V.; Dalnoki-Veress, K.; Forrest, J. A. *Eur. Phys. J.* **2003**, *11*, 191.
(31) Reiter, G.; Sommer, J.-U. *J. Chem. Phys.* **2000**, *112*, 4376.
(32) Sawamura, S.; Miyaji, H.; Izumi, K.; Sutton, S. J.; Miyamoto, Y. *J. Phys. Soc. Jpn.* **1998**, *67*, 3338.
(33) Taguchi, K.; Miyaji, H.; Izumi, K.; Hoshino, A.; Miyamoto, Y.; Kokawa, R. *J. Macromol. Sci., Phys.* **2002**, *B41*, 1033.
(34) Taguchi, K.; Miyaji, H.; Izumi, K.; Hoshino, A.; Miyamoto, Y.; Kokawa, R. *Polymer* **2001**, *42*, 7443.
(35) Sutton, S. J.; Izumi, K.; Miyaji, H.; Miyamoto, Y.; Miyashita, S. *J. Mater. Sci.* **1997**, *32*, 5621−5627.
(36) Taguchi, K.; Miyamoto, Y.; Miyaji, H.; Izumi, K. *Macromolecules* **2003**, *36*, 5208.
(37) Wang, M.; Braun, H.-G.; Meyer, E. *Polymer* **2003**, *44*, 5015.
(38) Wang, M.; Braun, H.-G.; Meyer, E. *Macromol. Rapid Commun.* **2002**, *23*, 853.
(39) Reiter, G. *J. Polym. Sci., Part B: Polym. Phys.* **2003**, *41*, 1869.
(40) Lotz, B.; Wittmann, J.-C. In *Materials Science and Technology*; Cahn, R. W., Haasen, P., Kramer, E. J., Eds.; VCH: New York, 1993; Vol. 12, p 80.
(41) Mareau, V. H.; Prud'homme, R. E. *Macromolecules* **2002**, *36*, 675.
(42) Eastmond, G. C. *Adv. Polym. Sci.* **2000**, *149*, 59.
(43) Ong, C. J.; Price, F. P. *J. Polym. Sci., Polym. Symp.* **1978**, *63*, 59.
(44) Ong, C. J.; Price, F. P. *J. Polym. Sci., Polym. Symp.* **1978**, *63*, 45.
(45) Pitt, C. G. In *Biodegradable Polymers as Drug Delivery Systems*; Chasin, M., Langer, R., Eds.; Marcel Dekker: New York, 1990; pp 71−120.
(46) Ciapetti, G.; Ambrosio, L.; Savarino, L.; Granchi, D.; Cenni, E.; Baldini, N.; Pagani, S.; Guizzardi, S.; Causa, F.; Giunti, A. *Biomaterials* **2003**, *24*, 2815.
(47) Bittiger, H.; Marchessault, R. H. *Acta Crystallogr.* **1970**, *B26*, 1923.
(48) Duvault, Y.; Gagnaire, A.; Gardies, F.; Jaffrezic-Renault, N.; Martelet, C. *Thin Solid Films* **1990**, *185*, 169.
(49) Aebi, U.; Pollard, T. D. *J. Electron Microsc. Technol.* **1987**, *7*, 29.
(50) Fully crystallized does not make reference to the degree of crystallinity, but to the fact that crystals have reached their maximum development in the originally fully amorphous sample.
(51) Kressler, J.; Wang, C.; Kammer, H. W. *Langmuir* **1997**, *13*, 4407.
(52) Iwata, T.; Doi, Y. *Polym. Int.* **2002**, *51*, 852.
(53) Brisse, F.; Marchessault, R. H. In *Fiber Diffraction Methods;* ACS Symposium Series No. 141; French, A. D., Garder, K. H., Eds.; American Chemical Society: Washington, DC, 1980; p 267.
(54) Kikkawa, Y.; Abe, H.; Iwata, T.; Inoue, Y.; Doi, Y. *Biomacromolecules* **2002**, *3*, 350.
(55) Davé, R. S.; Farmer, B. L. *Polymer* **1988**, *29*, 1544.
(56) Hocquet, S.; Dosière, M.; Thierry, A.; Lotz, B.; Koch, M. H. J.; Dubreuil, N.; Ivanov, D. A. *Macromolecules* **2003**, *36*, 8376.
(57) Reiter, G.; Vidal, L. *Eur. Phys. J. E* **2003**, *12*, 497.
(58) Huang, Y.; Xu, Z.; Ma, D.; Yang, J.; Mays, J. W. *Int. J. Polym. Anal. Charact.* **2004**, *8*, 383.

MA0482359